Supporting Information

for

Ion-induced transient potential fluctuations facilitate pore formation and cation transport through lipid membranes

D. Roesel[a,1], M. Eremchev[a,1], C. S. Poojari[b], J. S. Hub[b,2], and S. Roke[a,c,d,2]

[a]Laboratory for Fundamental BioPhotonics (LBP), Institute of Bioengineering (IBI), School of Engineering (STI), École Polytechnique Fédérale de Lausanne (EPFL), CH-1015 Lausanne, Switzerland; [b]Theoretical Physics and Center for Biophysics, Saarland University, 66123 Saarbrücken, Germany; [c]Institute of Materials Science and Engineering (IMX), School of Engineering (STI), École Polytechnique Fédérale de Lausanne (EPFL), CH-1015 Lausanne, Switzerland; and [d]Lausanne Centre for Ultrafast Science, École Polytechnique Fédérale de Lausanne (EPFL), CH-1015 Lausanne, Switzerland

[1] D.R. and M.E. contributed equally to this work.

[2]To whom correspondence may be addressed. Email: jochen.hub@uni-saarland.de or sylvie.roke@epfl.ch.

Table of Contents:

1. Materials and methods
   - 1.1. Chemicals and cleaning procedures
   - 1.2. Formation of freestanding lipid bilayers
   - 1.3. PVA-assisted GUV growth and transfer
   - 1.4. Second-harmonic imaging of FLMs
   - 1.5. Second-harmonic imaging of GUVs
   - 1.6. Setup and parameters of MD simulations
   - 1.7. Free energy calculations of membrane pore formation
   - 1.8. Simulation of ion permeation across an open pore
2. Supporting information
   - S1. Established and proposed membrane permeation models, review and discussion
   - S2. Conversion of SH intensity to electrostatic potential
   - S3. Spatial and temporal fluctuations in SH signal generated from a GUV
   - S4. Free energy calculations of membrane pore formation
   - S5. Formation of transient pores for membranes with different hydrophobic core structure
   - S6. Example SH GUV averaged time-lapses

S7. Inhomogeneities in translocation
S8. Estimate of membrane permeation times per Ca^{2+} in GUVs from MD simulations
S9. Computational comparison of Mg^{2+} and Ca^{2+} permeation
3. References

List of tables and figures

Table S1.Flux (permeation events per time) in simulations with a restrained open pore at an ion concentration of 1000 mM with different transmembrane potentials
Fig. S1. Established and proposed membrane permeability mechanisms
Fig. S2. Simulation snapshots of Ca^{2+} ions restrained in a POPC membrane
Fig. S3. PMFs of pore formation with or without Ca^{2+}/Mg^{2+} in absence of a transmembrane potential
Fig. S4. Spatial and temporal fluctuations in SH signal generated from a GUV
Fig. S5. Formation of transient pores for DOPC and DPhPC membranes
Fig. S6. SH signal timelapses measured from symmetric charged DOPC:DOPA 1:1 GUVs with added 5 mM divalent salt to the outside solution
Fig. S7. Membrane potential fluctuations induce inhomogeneous translocation of divalent cations
Fig. S8. Permeability of Ca^{2+} ions through POPC and POPC:POPS membranes at different transmembrane potential
Fig. S9. MD simulations of pore formation and ion permeation in presence of Mg^{2+} and Ca^{2+}

Materials and methods

Chemicals and cleaning procedures

1,2-diphytanoyl-sn-glycero-3-phosphocholine (DPhPC), 1,2-diphytanoyl-sn-glycero-3-phosphate (DPhPA), 1,2-dioleoyl-sn-glycero-3-phosphocholine (DOPC), 1,2-dioleoyl-sn-glycero-3-phosphate (DOPA), were purchased from Avanti Polar Lipids. $CaCl_2$ (99.999%), $MgCl_2$ (99.99%), $BaCl_2$ (99.999%), $CuCl_2$ (99.999%), KCl (99.999%), poly(vinyl alcohol) (PVA, Mw 146000 - 186000, >99%), bovine serum albumin (BSA, > 99%), glucose, sucrose, hexadecane ($C_{16}H_{34}$, 99.8%), hexane (C_6H_{14}, >99%), and chloroform (>99.8%) were purchased from Sigma-Aldrich. All chemicals were used as received. All aqueous solutions were made with ultra-pure water (H_2O, Milli-Q UF plus, Millipore, Inc., electrical resistance of 18.2 MΩcm). All aqueous solutions were filtered with 0.1 μM Millex filters. The coverslips used in the imaging were pre-cleaned with piranha solution (1:3 - 30% H_2O_2: 95-97% H_2SO_4) and thoroughly rinsed with ultrapure water. The chamber and Teflon films that were used in forming freestanding planar lipid bilayers were cleaned with ethanol, methanol, and chloroform and thoroughly rinsed with ultrapure water.

Formation of freestanding lipid bilayers

Freestanding horizontal planar lipid bilayers were formed following the procedure of Montal-Müller[1,2]. Two separated lipid monolayers on an air/water interface were opposed in a ~100 μm aperture in 25-μm thick Teflon film. Condensed lipid monolayers were formed on an air/water interface by depositing 3-8 μL of 10 mg/mL lipid solution in chloroform. Prior to forming a bilayer, the Teflon film was pre-painted on both sides with 1 μL of 99.5:0.5 vol% mixtures of hexane and an alkane solvent (squalene or hexadecane). We waited at least 10 minutes for hexane to evaporate. After bilayer formation, the Teflon film that contains the bilayer was positioned horizontally for imaging application. The presence of a bilayer was confirmed with white light imaging and electrical recordings. Capacitance and resistance measurements were taken with HEKA patch clamp amplifiers. Capacitance measurements were made with HEKA's built-in software based lock-in amplifier. Only bilayers with specific capacitance, C_m>0.7 μF/cm^2 and specific resistance, R_m~10^8 Ω·cm^2 were used.

PVA-assisted GUV growth and transfer

Giant unilamellar vesicles were formed by gel-assisted growth using polyvinyl alcohol (PVA) similar to the process described by Weinberger et al[3]. In brief, a 5% (w/w) solution of PVA in water was prepared and heated to 90 °C in a water bath. A rubber O-ring was bonded to a cleaned circular glass coverslip using a silicone elastomer (Kwik-Cast, World Precision Instruments) to form an open growth chamber and 50 μl of heated PVA was spread on the coverslip and dried for 30 minutes at 50 °C. Lipids dissolved in chloroform (5–10 μl, 1 mg/ml)

were then deposited on the dried PVA film and the chamber was placed under vacuum for 30 min in order to evaporate the chloroform.

The growth chamber was filled with a solution composed of 30 or 45 mM sucrose (with an addition of 100 μM phosphate buffer if required) in order to match the osmolarity of the observation solution. The growth chamber was observed using a light microscope (AmScope T490) in order to track the formation of vesicles. After the desired vesicle sizes were reached, typically in < 30 min, the GUVs were transferred into the observation chamber using a pipette. Due to the difference in density of the inside and outside solution, many GUVs precipitates to the bottom of the observation chamber and could either be imaged immediately or immobilized by pipette aspiration for more time-sensitive measurements.

An open observation chamber (Quick Change Chamber, Warner Instruments) was assembled separately using a cleaned coverslip, coated with bovine serum albumin (BSA) in order to prevent rupture of GUVs coming into contact with the glass surface, and rinsed with ultrapure water. It was then placed inside the SH microscope and filled with an observation solution composed of 30 mM glucose and 5 mM divalent salt. In some cases, 100 μM of phosphate buffer was added to the observation solution in order to maintain a constant relative charge of the anionic lipids.

Second-harmonic imaging of FLMs

SH images were obtained with a custom built wide-field second harmonic microscope that has been previously characterized in detail, see references [4,5]. The light source is Yb:KGW femtosecond laser (Pharos, Light Conversion Ltd.) delivering 190 fs pulses centered at 1030 nm with a 200 kHz repetition rate. The laser light is equally split with a 50:50 beam splitter into two counter-propagating beams. Each beam is passing through a 20 cm focal length lens and is incident at 45° with respect to the membrane. The chamber with a membrane is installed slightly out of the focus of both lenses to create a wide-field illumination of ~140 μm in diameter.

Polarisation of both beams can be controlled separately using a linear polarizer (Glan-Taylor polarizer, GT10-B; Thorlabs) and a zero-order half-wave plate (WPH05M-1030; Thorlabs). The average power at the sample plane was set between 100 mW to 240 mW for each arm which corresponds to a fluence of 50–120 GW/cm^2. The SH photons were collected with a long working distance 50× objective lens (Plan Apo NIR HR Infinity-Corrected Objective, 0.65 NA;Mitutoyo) in combination with a 18 cm tube lens (MT-L; Mitutuyo), a 900 nm short-pass filter (FES0900; Thorlabs), a 515 nm bandpass filter (FL514.5-10), and imaged with an electronically amplified intensified CCD camera (PiMAX-4; Princeton Instruments). The camera is gated at the frequency of the laser. Gating allows for photon detection within a <10 ns time window around the laser pulse arrival. The

accumulation time of all images was set to 500 ms with 20 subsequent frames being averaged.

Second-harmonic imaging of GUVs

The microscope is pumped by either femtosecond laser source (Femtolux 3, 1030 nm, 1 MHz, 220 fs) or a custom built optical parametric amplifier based on Femtolux 3 (670 - 1000 nm, 1 MHz, 23 - 50 fs). A combination of a lens (f = 25 cm, Thorlabs) and a 60x water immersion objective lens (Olympus LUMPFLN 60XW, NA 1.0) allows the laser beam to excite an area of 90 µm on a sample plane at normal incidence angle. The average power at the sample plane was set to 360 mW which corresponds to a fluence of 30 GW/cm^2. SH light is collected in the forward direction with a 60x objective lens (Olympus LUMFLN 60XW, NA 1.1) and imaged into an electronically amplified intensified CCD camera (EM-ICCD, PiMax-4, Princeton Instruments) with an 18 cm tube lens. A 750 nm short pass filter (FESH0750, Thorlabs) and a 515 nm band pass filter (FL514.5-10) were used in the detection path to remove the fundamental beam. The lateral resolution of the microscope is 400 nm. For polarization control a half-wave plate for the fundamental beam and a combination of a half-wave plate and a Glan–Taylor prism for detected light were used. SH images were recorded with a 1 s accumulation time and 5 subsequent images were averaged for better signal to noise ratio. For white-light imaging, the sample is illuminated from the top using a white light source and the linear scattered light is detected in the forward direction with the same objective lens.

Each GUV was first imaged by white light microscopy, in order to exclude multilamellar vesicles or vesicles with defects. These vesicles were excluded from analysis independently, without being observed by SH imaging, and therefore without any information about their potential brightness. After this initial screening, no further selection of vesicles was performed and each vesicle was measured by SH imaging, and subsequently analyzed. Each linearly polarized SH snapshot was processed in order to compensate for the shape of the excitation beam, as well as for the polarization direction of the excitation laser light. The processed image was then transformed from cartesian (x,y) to polar coordinates (R, φ) and an average SH signal for each value of phi was extracted by averaging in the r direction. After that, a 100°-wide region of the outline is selected, centered around the point where phi is aligned with the excitation polarization direction.

In this region, we set threshold intensity I_{th} as the maximum of the sum of read-noise and maximum dark current noise. This value determines the upper limit of the noise of the system. To determine I_{th} in counts, we calibrated the camera with the gain settings used during acquisition and obtained the number of counts/photo-electron[6]. The average domain size was determined using the spatial autocorrelation function (SACF), as described in detail

in Ref.[7]. A region of interest with a width of at least 2 times the FWHM of the SACF was used to compute the average domain intensity.

Setup and parameters of MD simulations

If not stated otherwise, simulations were set with the MemGen[8] web server with 256 lipids and 40 Charmm-modified TIP3P[9] water molecules per lipid. In simulations including ions, water molecules were replaced with ions to obtain the requested ion concentrations. If not stated otherwise, the simulations were carried out with the Charmm36 lipid force field with electronic continuum correction (Charmm36-ECC), a Charmm36 variant with improved lipid–ion interactions[10–16]. ECC-ion parameters for Ca^{2+}, Mg^{2+}, K^+ and Cl^- ions were taken from Refs[10–13]. Electrostatic interactions were described with the particle-mesh Ewald method[17]. Lennard-Jones interactions were truncated at 1.2 nm, while the force was gradually switched off between 1 and 1.2 nm. The temperature was controlled at 310 K using velocity rescaling, thereby coupling membrane and solvent to separate heat baths (τ = 1 ps)[18]. The pressure was kept at 1 bar using the semi-isotropic Parrinello-Rahman barostat[19]. No hydrogen mass repartitioning (HMR) was applied, and an integration of 2 fs was used. The geometry of water molecules was constrained with the SETTLE algorithm[20]. Other bonds involving hydrogen atoms were constrained with LINCS[21]. The simulations were carried out with the GROMACS simulation software, version 2021.[22]

PMF calculations of pore formation over membranes of DOPC and DPhPC were carried out in absence of ions and using the regular Charmm36 lipid force field without ECC corrections[14]. The systems were set up with MemGen[8] with 162 lipids and 40 Charmm-modified TIP3P[9] water molecules per lipid. Hydrogen mass repartitioning was used, allowing a time step of 4fs. All other parameters were chosen as described above. The transmembrane potential was implemented using an external electric field E_z along the *z*-direction (membrane normal)[23]. Here, E_z was chosen such that $E_z L_z$ equals the transmembrane potential, where L_z is the box dimension in *z* direction.

Free energy calculations of membrane pore formation

Potentials of mean force (PMFs) of pore formation were computed along the chain coordinate ξ_{ch}, a reaction coordinate that quantifies the degree of connectivity of a polar defect over the lipid membrane[24,25]. In brief, ξ_{ch}, is defined with the help of a cylinder that spans the lipid membrane. The cylinder is decomposed into N_s slices. ξ_{ch}, is defined by the fraction of slices that are filled by polar heavy atoms. In this study, water oxygen atoms as well as the oxygen atoms of lipid phosphate groups contributed to ξ_{ch}. By pulling the simulation system along ξ_{ch}, the slices are filled one-by-one, thereby forming a continuous polar defect over the membrane. Critically, restraints along ξ_{ch} impose merely a certain

degrees of connectivity of the defect, while the radius, shape, and molecular content of the defect is chosen the MD simulation model (force field) at the given simulation conditions (temperature, ensemble etc.). For instance, the most favorable degree of membrane bending along the pore rim or the relative ratio of water, ions, and headgroups inside the pore are –for a given ξ_{ch}– decided by the force field and simulation conditions.

The use of a cylinder for defining ξ_{ch} ensures the locality of the defect in the membrane plane, thereby avoiding that two laterally displaced partial defects, one in the upper leaflet and one in the lower leaflet, would be misinterpreted as a continuous transmembrane defect. Such misinterpretation would lead to undesired hysteresis effects and a free energy barrier of pore nucleation, if present, would be integrated out. Critically, the pore radius is not controlled by the cylinder radius R_{cyl} but instead selected by the force field at the given simulation conditions (temperature, ensemble etc). The lateral position of the cylinder is dynamically defined, thereby allowing the cylinder to follow the defect as it travels laterally in the membrane plane. Harmonic restraints along ξ_{ch} as required or umbrella sampling simulations have been implemented into an in-house modification of GROMACS 2021, which is freely available at https://gitlab.com/cbjh/gromacs-chain-coordinate. Technical details on ξ_{ch} have been described in Ref. [24]. We previously showed that PMF calculations along ξ_{ch} do not suffer from hysteresis problems, in contrast to PMF calculations along several other reaction coordinates of pore formation.[26]

Starting from an equilibrated membrane, a pore was introduced using constant-velocity pulling from ξ_{ch} = 0.1 to ξ_{ch} = 1 over 100 ns, using a force constant of 3000 kJ/mol along ξ_{ch}. The coordinate ξ_{ch} was defined with a cylinder with radius R_{cyl} = 0.9 nm, decomposed into slices with a thickness of d_s = 0.1 nm. Upon the addition of the first polar atom, a slice was considered as being filled by 75%. The number of slices N_s, and thereby the length of the cylinder $N_s d_s$, was chosen such that $\xi_{ch} \approx 0.2$ for the flat unperturbed membrane, implying that approximately 20% of the slices are filled by polar atoms in the unperturbed membrane.

The PMFs were computed using umbrella sampling with 27 umbrella windows. Starting frames for umbrella sampling were taken from the constant-velocity pulling simulation. Since the conformational sampling is more challenging at larger ξ_{ch} values compared to smaller ξ_{ch} values, we used the following non-equidistant spacing for the reference positions of the umbrella windows: 0.065 through 0.625 in steps of 0.08, and 0.64 through 1.0 in steps of 0.02. For reference positions smaller or larger than 0.7 we used force constants of 5000 or 10000 kJ/mol, respectively. Each window was simulated for 100 ns. The first 20 ns were omitted for equilibration, and the PMFs were computed with the weighted histogram analysis method, as implemented in the gmx wham module of

GROMACS[27,28]. Statistical errors were estimated using 50 rounds of bootstrapping complete histograms[27].

Simulation of ion permeation across an open pore

Systems for the simulation of Ca^{2+} and Mg^{2+} permeation across an open pore were set up as described above. Water molecules were replaced with Ca^{2+}, Mg^{2+}, and Cl^- ions to obtain $CaCl_2$ or $CaMg_2$ concentrations of 1000 mM. Here, we used large ion concentrations to improve the statistics of permeation events. The simulations were carried out with the Charmm36-ECC force field[10–16]. After equilibration, a pore was induced by pulling along ξ_{ch} from 0.1 to 1 over 100 ns using a force constant of 3000 kJ/mol. Then, the system was restrained at $\xi_{ch} = 1$ with a harmonic restraint along ξ_{ch} with a force constant of 10000 kJ/mol, and then simulated for 500 ns. The permeability of the pore was obtained by counting the number N_p of Ca^{2+} or Mg^{2+} permeation events across the pore (in any direction). The permeability was computed as $p = N_p/c$, where c denotes the Ca^{2+} concentration. This relation takes into account that we did not simulate with a Ca^{2+} concentration gradient but instead with equal concentration on both sides of the membrane, thus allowing permeation events in both directions.

PMFs of pulling Ca^{2+} across the membrane

To test whether a partly hydrated Ca^{2+} ion could permeate the membrane (see section S1, Fig. S2), we computed the PMF for Ca^{2+} translocation using the z-position (membrane normal) of a Ca^{2+} ion relative to the lipid center of mass as reaction coordinate. The PMF was computed using umbrella sampling and using the Charmm36-ECC force field[10–16]. Reference positions of umbrella windows were separated by 0.05 nm. The umbrella force constant was set to 1000 kJ/mol nm^{-1}. Each window was simulated for 10 ns, while the first 5 ns were discarded for equilibration. The PMF was computed using WHAM[27,28], and the statistical errors using 50 rounds of Bayesian bootstrapping of complete histograms[27]. The initial frames for umbrella sampling were generated using two different setups yielding two different PMFs: (i) the Ca^{2+} ion was inserted at the reference position of the respective umbrella window, and the energy of the system was minimized. Since this setup is by design symmetric with respect to the membrane center, the PMF was symmetrized and the free energy at the two water compartments was set to zero. (ii) Initial frames were taken from a steered MD simulation pulling Ca^{2+} from z = -2.6 nm to z = 2.6 nm over 200 ns of simulation. This setup leads to a massively non-symmetric PMF since the Ca^{2+} drags a large water defect across the membrane. Hence, the PMF was not symmetrized.

S1. Established and proposed membrane permeation models, review and discussion

The established (A-D) and here proposed (E) mechanisms of unassisted ion transport through lipid membranes are shown in Fig. S1. The thermal pore model (Fig. S1A) states that thermal fluctuations in the membrane structure lead to the opening of transient pores[29,30]. These pores are lined with lipid headgroups and water, allowing the ion to translocate without having to overcome the energy barrier of partitioning into the nonpolar membrane phase. The solubility diffusion model (SDM, Fig. S1B) describes the permeation process as the combination of two processes: the ability of molecules to partition into the hydrophobic interior of the membrane[31] (solubility) and their movement down the concentration gradients[32] (diffusion). The lipid flipping model (Fig. S1C) assumes that ion permeation is facilitated by the thermally induced translocation of individual lipids which carry an ion associated to their headgroup in the process[33]. The ion-induced defect model (Fig. S1D) states that the interaction of the ion with the bilayer creates a local membrane deformation, which lowers the free energy barrier for the ion without forming a complete hydrophilic pore[34–36].

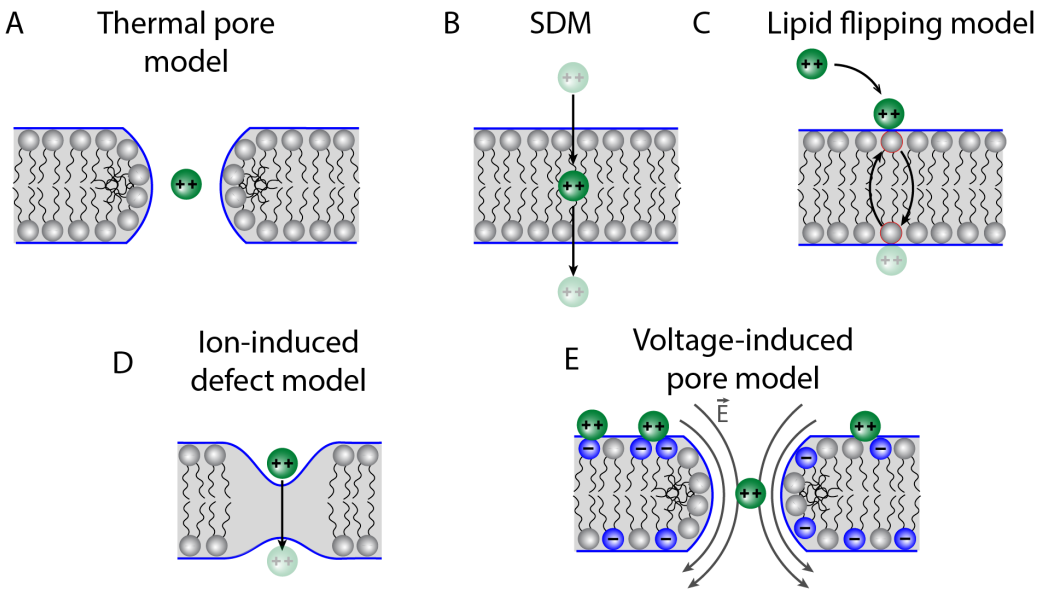

Figure S1. Established and proposed membrane permeability mechanisms. (A) Thermal fluctuations create a transient pore. (B) Solubility diffusion model. (C) Lipid flipping carrier model. (D) Ion-induced defect model. (E) Voltage-induced pore model proposed in this work.

Although certain aspects of our observations can be partially accounted for by some of these models, none of these established mechanisms are fully compatible with our experiments and simulations. The free energy for the unassisted formation of thermal pores

in absence of a transmembrane potential is too large to rationalize the experimental permeation rates (Fig. 2C). In addition, the thermal pore model does not explain the varying permeabilities of different divalent ions (Fig. 2A). While the lipid flipping mechanism is consistent with monovalent cation permeation experiments done on membranes with a high content of monoacyl fatty acids[37], it fails to accurately describe ion permeation for membranes which exhibit a lower rate of lipid flipping[38,39].

The SDM is excluded by the large negative solvation free energy of divalent ions in the range of –1250 to –2395 kJ/mol,[40] rendering the translocation of a bare ion across the hydrophobic membrane core energetically unfeasible. To confirm that the membrane is not permeated by a dehydrated Ca^{2+} ion, we carried out a series of simulations with Ca^{2+} ions restrained at various penetration depths inside the membrane core. These simulations were carried out with the Charmm36-ECC model, suggesting that the simulations implicitly account for Ca^{2+} stabilization in the hydrophobic core by electron polarization. As expected from the large negative hydration free energy of Ca^{2+} of –1505 kJ/mol, the ions were rapidly solubilized by dragging water into the membrane, in contrast with the expectations from the SDM model (Fig. S2, A–D). These simulations further exclude Ca^{2+} permeation via lipid flip-flop across a dry defect.

The exclusion of a bare Ca^{2+} ion from the membrane core (previous paragraph) does not exclude the possibility of a SDM with partly hydrated Ca^{2+}. To test whether the permeation of a partly hydrated Ca^{2+} is energetically accessible without forming a continuous transmembrane defect, we computed the PMF for Ca^{2+} permeation across a POPC membrane using the *z*-position of Ca^{2+} (membrane normal) as reaction coordinate, similar to previous studies[34,41]. The PMFs were computed using umbrella sampling with two different setup protocols: (i) Ca^{2+} were inserted at increasing *z*-positions, thereby obtaining a PMF that is symmetric with respect to the membrane center (Fig. S2E, green line); (ii) after pulling Ca^{2+} across the membrane from the lower to the upper water compartment, thereby obtaining a non-symmetric PMF because the pulled Ca^{2+} drags a large water defect into the membrane that persists even after the Ca^{2+} is pulled beyond the membrane center (Fig. S2E, orange line). Notably, the free energy of pore formation in POPC ΔG_{pore} of ~90 kJ/mol (Fig. 1C) is lower as compared to the barrier revealed by the PMF after Ca^{2+} pulling of ~135 kJ/mol (Fig. S2E, orange line). This finding strongly suggests that Ca^{2+} permeation proceeds via the formation of a continuous transmembrane defect and not by the permeation of a partly hydrated Ca^{2+}, as previously also found for monovalent ions[34]. In addition, the finding demonstrates that pulling along the *z*-position of Ca^{2+} perturbs the membrane more strongly than required for Ca^{2+} permeation, implying that the *z*-position of Ca^{2+} is a poor reaction coordinate for Ca^{2+} permeation. Critically, the PMF obtained after inserting Ca^{2+} underestimates the barrier for Ca^{2+} permeation because the two branches (at $z < 0$ nm and z

> 0 nm in Fig. S2E, green line) represent two distinct regions of conformational space, characterized by a water defect (i) connected with the lower water compartment (z < 0 nm, Fig. S2A/B) or (ii) connected with the upper water compartment (z > 0 nm, Fig. S2C/D). These two branches are separated by a "hidden barrier"[42] that is integrated out upon projecting the free energy landscape onto the Ca^{2+} *z*-coordinate. Overcoming this hidden barrier likely involves the formation of a transmembrane defect, as quantified by our PMFs of pore formation (Fig. 1C). Together, this analysis renders a SDM with partly hydrated Ca^{2+} ions unlikely and suggests that the formation of a transmembrane defect is the limiting step of Ca^{2+} permeation.

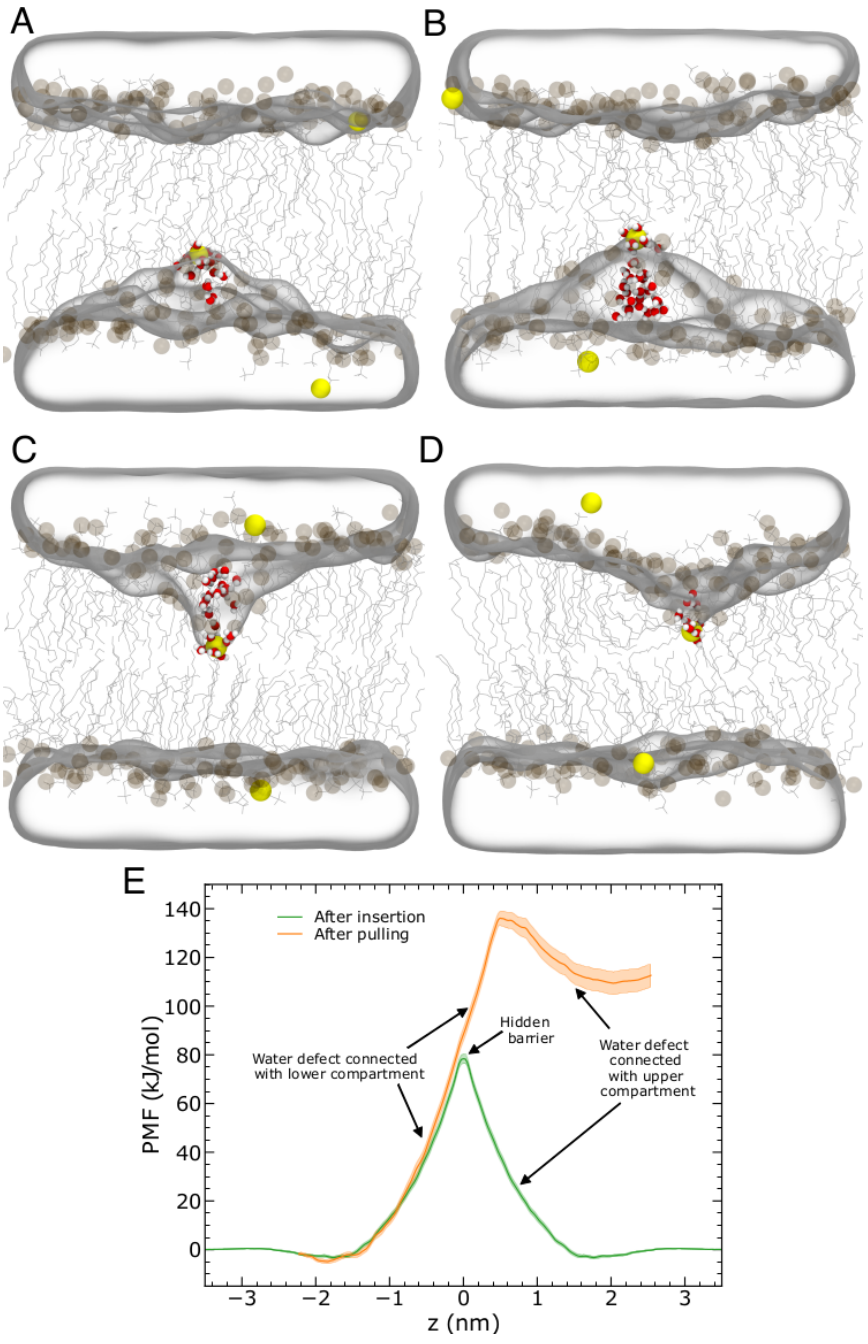

Figure S2: Simulation snapshots of Ca^{2+} ions restrained in a POPC membrane. Snapshots (A,B,C,D) reveal water dragged into the POPC membrane by an Ca^{2+} ion restrained at varying depths inside the membrane. The Ca^{2+} ion and lipid phosphorus atoms are rendered as yellow and brown spheres respectively. Lipid tails are shown as grey lines. Water is represented as a transparent surface and water molecules dragged into the hydrophobic core of the membrane are rendered as van der Waal spheres. For image rendering, bulk water in the z-direction was limited to ~1.0 nm from the upper and lower leaflet lipid phosphorus atoms. (E) PMFs of Ca^{2+} translocation across the membrane normal *z* without a previously formed pore computed either by inserting Ca^{2+} at increasing z-positions along the membrane normal (green), or after pulling Ca^{2+} from the lower to the upper water reservoir (orange).

To test whether the ion-induced defect model explains divalent ion transport (Fig. S1D), we computed free energies of pore formation ΔG_{pore} without transmembrane potential but in presence of an increasing Ca^{2+} or Mg^{2+} concentration. If the ion-induced defect model would hold, increasing concentration of divalent ions would destabilize the membrane and, thereby, decrease ΔG_{pore}. Such mechanism was previously found upon the addition of membrane-active substrates such as polyarginines[43] or cationic polymers[44]. However, in variance with expectations from the ion-induced defect model, the addition of divalent ions increased ΔG_{pore} in a concentration-dependent manner (Fig. S3), demonstrating that Ca^{2+} or Mg^{2+} make the membrane even more stable against pore formation. The divalent ions likely increased ΔG_{pore} because they may bridge lipid–lipid interactions, thereby (i) rendering the intrinsic curvature of the lipids effectively more negative, which is incompatible with the large positive curvature along the pore rim and (ii) disfavoring the breaking of lipid–lipid interactions as required for pore formation.

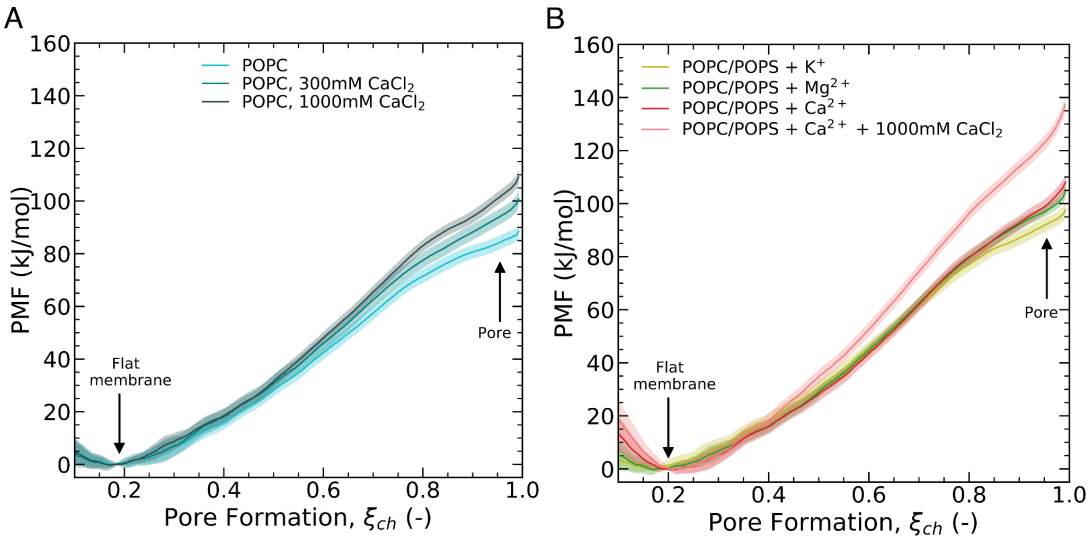

Figure S3: PMFs of pore formation with or without Ca^{2+}/Mg^{2+} in absence of a transmembrane potential. (A) PMFs of pore formation over POPC membranes without ions (light blue), with 300 mM $CaCl_2$ (medium blue) or with 1000 mM $CaCl_2$ (dark blue). (B) PMFs over a POPC:POPS 1:1 mixture in presence of K^+ neutralizing ions (yellow), Mg^{2+} neutralizing ions (green), Ca^{2+} neutralizing ions (dark red), or with at 1000 mM $CaCl_2$ (light red).

The PMFs reveal that interactions of lipids with Ca^{2+} or with Mg^{2+} render the membrane more stable against pore formation, as evident from the increased free energies of pore formation at $\xi_{ch} \approx 1$. This effect is likely explained by the formation of lipid–Ca^{2+}–lipid bridges that stabilize a planar head group structure and, hence, disfavor pore formation. The PMFs were computed with the Charmm36-ECC force field.

S2. Conversion of SH intensity to electrostatic potential

For a lipid membrane with two interfaces (*i* = 1 or 2), the total emitted SH intensity $I(2\omega, x, y)$ is related to the surface potential (Φ_0) and can be expressed as[5,7,45]:

$$I(2\omega, x, y) \propto I(\omega, x, y)^2 \left| \chi_{s,1}^{(2)}(x, y) - \chi_{s,2}^{(2)}(x, y) + \chi_s^{(3)'} f_3 \left(\Phi_{0,1}(x, y) - \Phi_{0,2}(x, y) \right) \right|^2 \quad \text{(S1)}$$

where ω is the frequency of the fundamental beam, x and y are the spatial coordinates, $\chi_{s,i}^{(2)}$ (*i* = 1 or 2) are the second-order surface susceptibilities, $\Phi_{0,i}$ (*i* = 1 or 2) are the surface potentials of each leaflet of the membrane, $\chi_s^{(3)'}$ is the effective third-order surface susceptibility of the water, and f_3 is an interference term where $f_3 = 1$ for the case of a transmission experiment. For the case of lipid membranes with a symmetric lipid composition, $\chi_{s,1}^{(2)}$ is equal to $\chi_{s,2}^{(2)}$, on average. Due to the fact that $\chi_{s,i}^{(2)}$ does not change significantly upon the addition of ions and $\chi_s^{(3)'}$ is at least two orders of magnitude larger than $\chi_{s,i}^{(2)}$[5], the SH signal observed in our images can be attributed to the difference in membrane surface potential $\Delta\Phi_0 = \Phi_{0,1}(x, y) - \Phi_{0,2}(x, y)$ and Eq. (S1) can therefore be reduced to:

$$I(2\omega, x, y) \propto I(\omega, x, y)^2 \left| \chi_s^{(3)'} \Delta\Phi_0(x, y) \right|^2. \quad \text{(S2)}$$

Based on Eq. (S2), SH intensity is converted to a surface potential difference $\Delta\Phi_0$ by recording SH images of FLMs as a function of external electric voltage across the membrane[5,7]. In order to convert SH intensity of GUVs into the membrane potential, the FLMs and GUVs are prepared from the same lipid composition and imaged with the same acquisition and illumination conditions. After that, the average SH intensities from both systems are compared and used to normalize the SH response of GUVs to membrane potential.

S3. Spatial and temporal fluctuations in SH signal generated from a GUV

Fig. S4A shows the SH image of a DPhPC:DPhPA 1:1 GUV in contact with 5 mM $CaCl_2$ salt solution in the XX polarization configuration. The right part of the image was converted to a polar coordinate system to study the spatio-temporal evolution of the SH signal (Fig. S4B).

The image in polar coordinates was normalized by $cos^2(\theta)$ for an acceptance angle θ of up to 100 degrees (to compensate for the polarization dependence of the SH process). Fig. S4C shows an example of a normalized GUV outline with domains of brighter and darker spots, which are directly connected to mechanical deformations of the membrane and the strength of ion binding. These results show that the binding of divalent cations does not happen homogeneously along the GUV surface. Fig. S4D shows the time evolution of the SH signal at a single position along the outline, which shows temporal fluctuations. Local membrane deformations caused by ion binding are highly relevant for unassisted ion transport, which is heavily influenced by any changes in the local chemical structure of the bilayer.

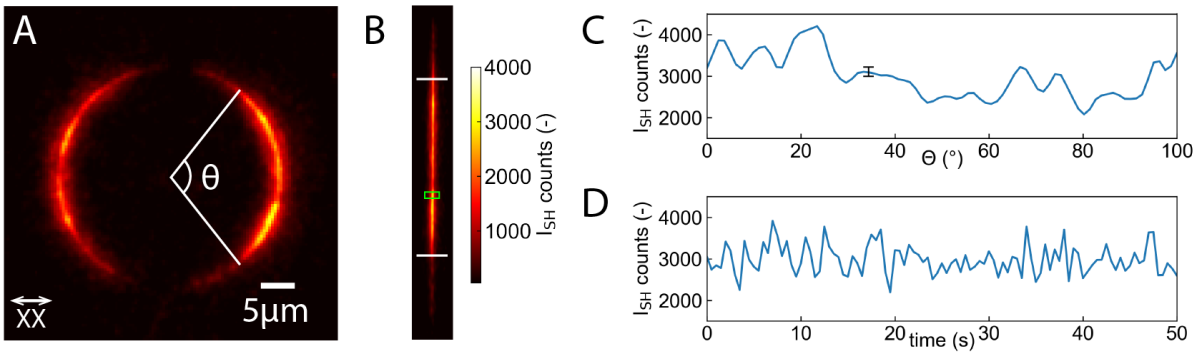

Figure S4: Spatial and temporal fluctuations in SH signal generated from a GUV. (A) SH image of a DPhPC:DPhPA 1:1 GUV in contact with a 5 mM $CaCl_2$ salt solution. θ indicates the angular portion of the image used for further processing. (B) Extracted portion of the GUV outline converted to a polar coordinate system, which is analyzed to study the spatio-temporal heterogeneities of the SH signal. (C) Normalized GUV outline extracted from B which shows fluctuations in SH signal along the membrane. (D) The time evolution of SH signal in selected ROI (green box in B) which shows temporal fluctuations of SH signal. The error bar represents the accuracy of a single measurement.

S4. Formation of transient pores for membranes with different hydrophobic core structure

To reveal the effect of the hydrophobic core on pore formation, we performed MD simulations with DPhPC and DOPC membranes. Fig. S5 shows the PMFs of pore formation extracted from the simulations, the molecular structure of the lipids, as well as the MD snapshots of an open pore for both cases. The free energy cost ΔG_{pore} of forming a pore across a DPhPC membrane is increased by ~40 kJ/mol compared to a DOPC membrane, in line with the absence of ion permeation over GUV membranes with lipids with phytanoyl tails, as used to measure transmembrane potentials in the presence of Cu^{2+}, Ca^{2+}, Ba^{2+}, and Mg^{2+} (cf. Fig. 2B). Structurally, the increased ΔG_{pore} in DPhPC is rationalized by (i) the tight

packing of the bulky phytanoyl tails and (ii) by the increased tail-to-headgroup volume ratio compared to DOPC, which leads to unfavorable packing of DPhPC lipids at the large positive curvature along pore rim[25]. These results show that pores form in DOPC with a much higher probability than in DPhPC membranes.

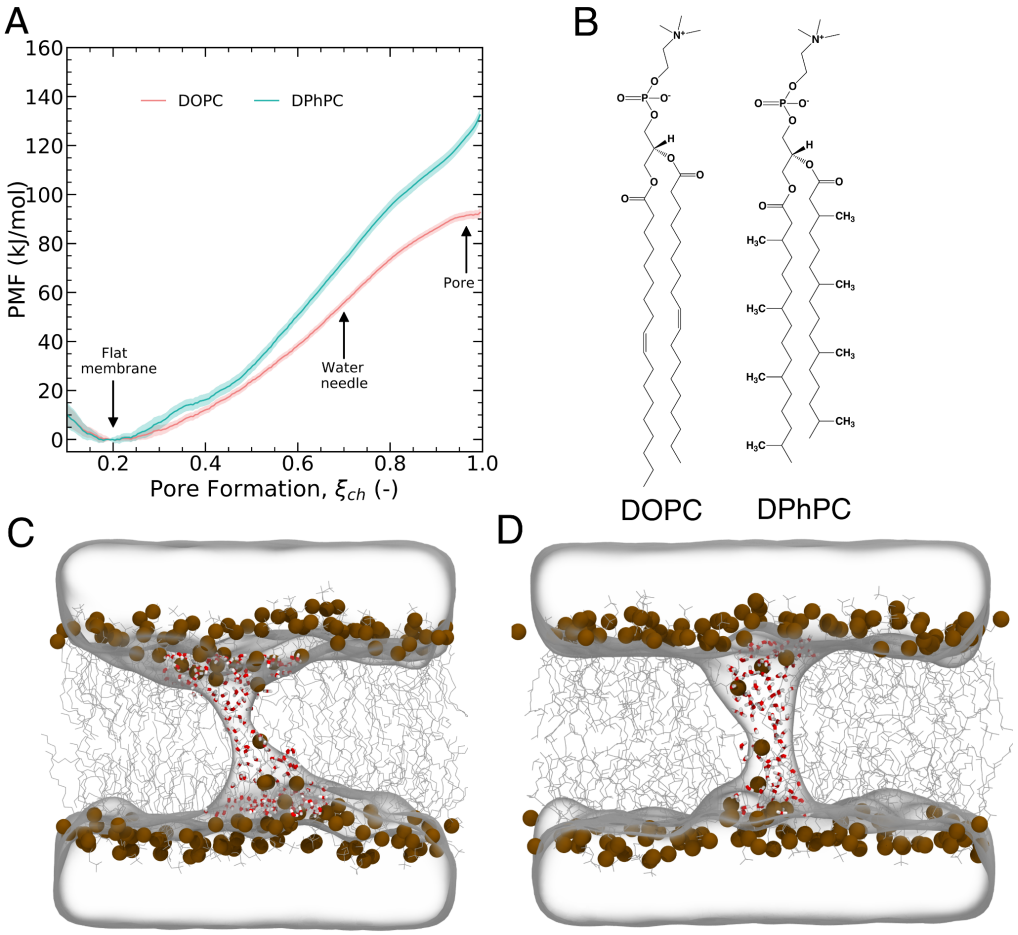

Figure S5: Formation of transient pores for DOPC and DPhPC membranes. (A) PMFs of pore formation across membranes of DOPC (red) and DPhPC (blue). The PMFs were computed with the Charmm36 lipid force field (without electronic continuum correction) without transmembrane potentials. (B) Molecular structures of DOPC and DPhPC lipids. (C,D) The MD snapshots of an open pore at ξ_{ch}≈1 in (C) DOPC and (D) DPhPC membranes respectively. Lipid phosphorus atoms are rendered as brown spheres and lipid tails as lines. Water molecules inside the membrane are represented as sticks and bulk water as a transparent surface.

S5. Example of averaged SH time-lapses of GUVs

The time constants for ion translocation shown in Fig. 2A were extracted from time lapse SH images obtained from individual GUVs and averaged across multiple experiments (>10 GUVs per ion). Fig. S6 shows typical averaged SH traces obtained for each divalent cation for GUVs composed of a DOPC:DOPA 1:1 molar ratio. Each dot in Fig. S6 represents the averaged SH intensity of a single GUV recorded over a time frame of 60 s. SH values were

extracted from images by averaging the SH signal along the normalized GUV outline with an acceptance angle of 100-120 degrees. Throughout our experiments we have not observed a SH decay for Mg^{2+} ions (Fig. S6A). GUVs with Ba^{2+} salt outside show a slow SH signal decay as shown in Fig. S6B. In all time-lapses the full decay time was significantly longer than the experiment time (which is typically not more than 3 hours). Line extrapolation was used to extract the full time of SH signal decay. Fig. S6C and D show the SH signal decay for GUVs in contact with Cu^{2+} and Ca^{2+} ions. A fast decay for both ions is observed with Cu^{2+} having faster decay time compared to Ca^{2+}. The same trend was observed when the experiments were repeated with the PS head group of lipids instead of PA. For comparison, Fig. S6D shows the SH signal from a GUV composed of branched DPhPC:DPhPA lipids in contact with Ca^{2+} ions which does not show any SH decrease.

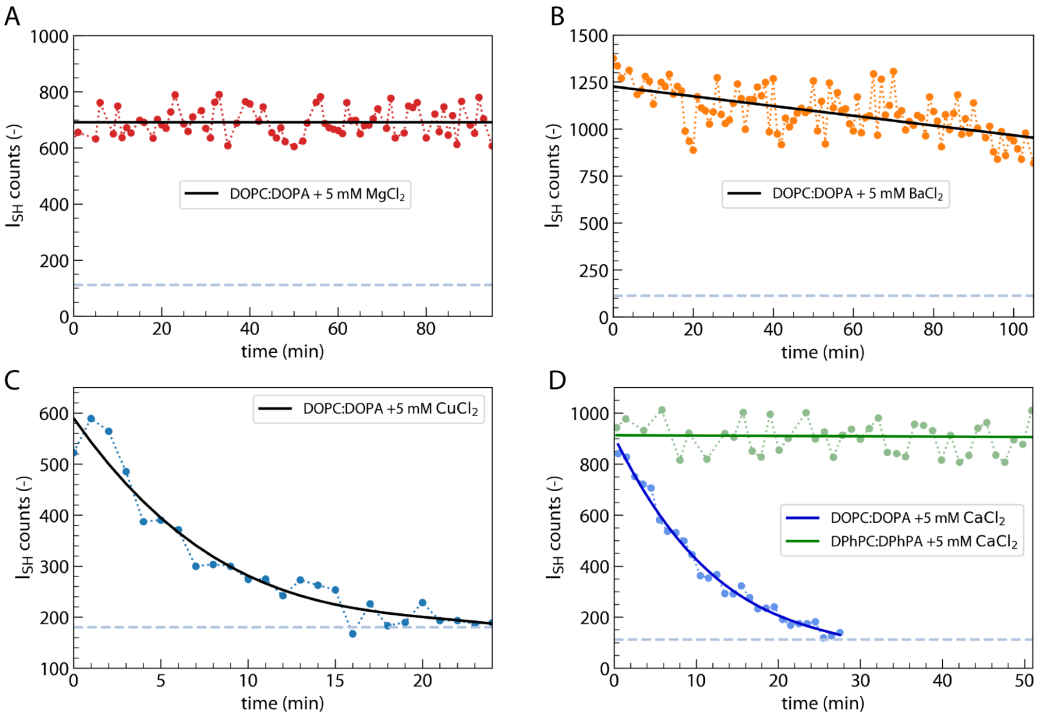

Figure S6: SH signal timelapses measured from symmetric charged DOPC:DOPA 1:1 GUVs with added 5 mM divalent salt to the outside solution. (A) SH signal stays constant after adding $MgCl_2$ for > 100 minutes. (B) SH signal decays slowly after adding $BaCl_2$ (C) and (D) Signal decay for GUVs in contact with Cu^{2+} and Ca^{2+}. Both ions permeate fast through a lipid membrane. Green data in (D) shows the data for GUVs formed from DPhPC:DPhPA 1:1 in contact with Ca^{2+} ions. No permeation is observed for this lipid composition. Light dashed line shows the noise level.

S6. Inhomogeneities in translocation

Translocation of divalent cations through a DOPC:DOPA membrane is not homogeneous along the GUV surface – in agreement with the transient nature of the transmembrane potential fluctuations. To demonstrate this, we analyzed the signal decrease for multiple

regions of interest along the GUV outline of a SH image (Fig. S7A and B, green ROI), we built a spatial map of translocation times. Fig. S7C shows such maps for translocation of Ca^{2+} and Cu^{2+} ions. From here it is visible that local time constants of ion translocation vary two- to threefold for different positions on the GUV surface. These results imply that local fluctuation of membrane potential leads to fluctuation in permeation times.

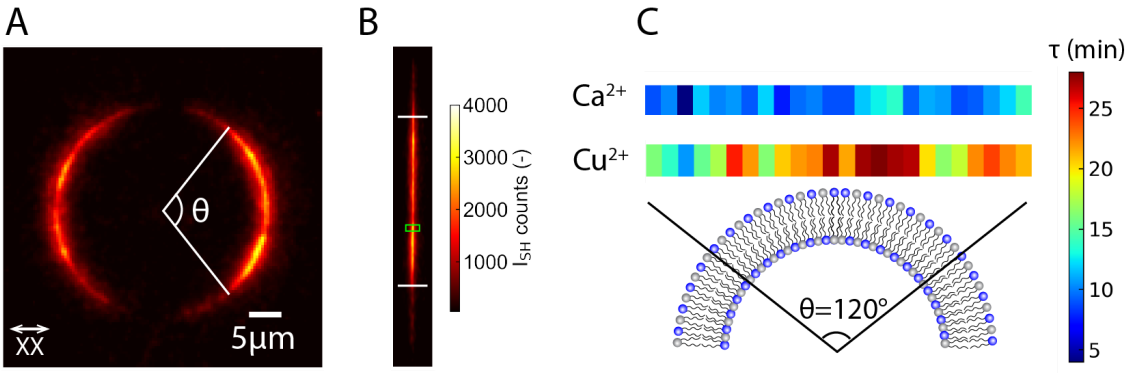

Figure S7: Membrane potential fluctuations induce inhomogeneous translocation of divalent cations. (A) SH image of a DPhPC:DPhPA 1:1 GUV in contact with a 5 mM $CuCl_2$ salt solution. Θ indicates the angular potion of the image used for further processing. (B) Extracted portion of the GUV outline converted to a polar coordinate system, which is analyzed to study the spatio-temporal heterogeneities of the SH signal. (C) Spatial map of translocation times for 1 µm wide regions of interest along the GUV outline for Cu^{2+} and Ca^{2+} which shows inhomogeneities in translocation.

S7. Membrane permeation time estimation per Ca^{2+} ion in GUVs from MD simulations

The PMFs provide the probability for forming a pore in the simulation system with the simulation membrane area A_{sim} = 77 nm^2. Since the probability of forming a pore (P_{pore}) scales with the membrane area, the probability for forming a pore in the GUV with the area A_{GUV} is

$$P_{pore} = \frac{A_{GUV}}{A_{sim}} e^{-\Delta G_{pore}/k_B T}, \qquad \text{(S3)}$$

where ΔG_{pore} is the free energy of the pore relative to the flat membrane, as taken from the PMFs of pore formation (Fig. S8A). Further, k_B is the Boltzmann constant and T the simulation temperature of 310 K. For the GUV surface area, we used $A_{GUV} = 4\pi R_{GUV}^2$ with R_{GUV} = 10 µm. Since a continuous transmembrane defect is present at $\xi_{ch} \geqq 0.85$, we took ΔG_{pore} as well as the uncertainty $\delta\Delta G_{pore}$ from the PMF at $\xi_{ch} \approx 0.85$. Since the PS headgroups were neutralized at a local Ca^{2+} concentration of 300 mM in our simulations, we

assumed that the local ion concentration under experimental conditions is approximately 300 mM. Hence, the flux (F_{GUV}) over the entire GUV membrane is:

$$F_{GUV} = 0.3 \cdot F_{1000} P_{pore}, \quad \text{(S4)}$$

where the factor 0.3 accounts for the smaller concentration of 300 mM compared to 1000 mM, and F_{1000} is the flux across an open pore taken from MD simulations (Table S1). The time per ion permeation over the entire GUV membrane is:

$$\tau_{perm} = 1/F_{GUV} \quad \text{(S5)}$$

The statistical error of τ_{perm} is dominated by the uncertainty $\delta\Delta G_{pore}$ of the PMF at $\xi_{ch} \approx 0.85$. Namely, $\delta\Delta G_{pore}$ translates into an uncertainty of τ_{perm} by a factor of $\delta f = \exp(\delta\Delta G_{pore}/k_B T)$. As upper and lower bounds for τ_{perm}, we used $\tau_{perm} \cdot \delta f$ and $\tau_{perm}/\delta f$, where δf was in the order of $\delta f \approx 3$. In addition to the statistical uncertainty taken from the PMFs, uncertainties in the force field may translate into substantial uncertainties in the estimated rates. As a numerical example, modified free energies of pore formation by 5 or 10 kJ/mol, translate into modified permeation rates by factors of 7 or 48, respectively. Hence, whereas the trends of ΔG_{pore} values with increasing transmembrane potentials are reliable, the τ_{perm} values obtained from the MD simulations should, at best, be interpreted as an order-of-magnitude estimate (Fig. S8B).

The experimental value of free energy of pore formation was obtained by:

$$\Delta G_{exp} = -kT \cdot ln\left(\frac{A_{sim}}{0.3 \cdot A_{GUV} \cdot \tau_{exp} \cdot F_{1000}}\right), \quad \text{(S6)}$$

using experimentally extracted translocation time τ_{exp} and simulated value of ion flux F_{1000}. The values computed for ΔG_{exp} are plotted in Fig. 2C.

Table S1: Flux (permeation events per time) in simulations with a restrained open pore at an ion concentration of 1000 mM with different transmembrane potentials. Simulations were carried out with the Charmm36-ECC force field.

	ΔU (mV)	$F_{1000}(Ca^{2+})$ (μs^{-1})	$F_{1000}(Mg^{2+})$ (μs^{-1})
POPC	0	1.66	-
POPC	200	8	-
POPC	400	58	-
POPC	600	9740	-
POPC:POPS	0	0.42	-
POPC:POPS	200	10	8
POPC:POPS	400	22	30
POPC:POPS	600	100	622

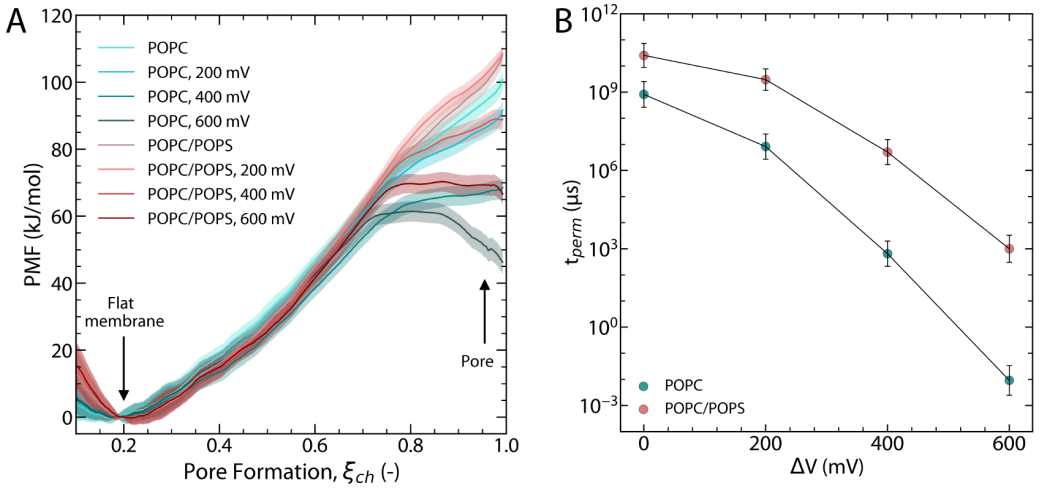

Figure S8: Permeability of Ca^{2+} ions through POPC and POPC:POPS membranes at different transmembrane potential. (A) PMFs of pore formation across membranes of POPC or POPC:POPS 1:1. The decrease of ΔG_{pore} with increasing voltage is independent of lipid composition. However, the addition of POPS increases ΔG_{pore} because POPS lipids exhibit a smaller head-to-tail volume ratio compared to POPC, which is incompatible with the large positive curvature along the pore rim.[25] (B) Computed permeability times of a single Ca^{2+} ion through POPC and POPC:POPS for GUVs of 10 µm radius as a function of transmembrane potential, computed from MD simulations and translated to a GUV membrane area.

S8. Computational comparison of Mg^{2+} and Ca^{2+} permeation

Additional support for electric field-induced ion permeation was given by simulations of Mg^{2+} and Ca^{2+} permeation at membrane potential magnitudes of 0, 200, 400, and 600 mV. Upon replacing Ca^{2+} with Mg^{2+}, ΔG_{pore} marginally decreases (Fig. S9A,B), implying a slightly increased propensity of pore formation for a certain membrane potential. Given an open pore, the Mg^{2+} permeation increased relative to Ca^{2+} permeation, likely owing to weaker binding of Mg^{2+} to the lipid head groups as compared to Ca^{2+} (Fig. S9C,D). Consequently, if Mg^{2+} and Ca^{2+} would be at membranes with the same transmembrane potential, the simulations suggest an increased flux of Mg^{2+} as compared to Ca^{2+}, in contrast to our experimental findings (Fig. 2A). These simulations therefore suggest that the experimentally detected low Mg^{2+} permeability is a consequence of lower transmembrane potential in the presence of Mg^{2+} (Fig. 2B).

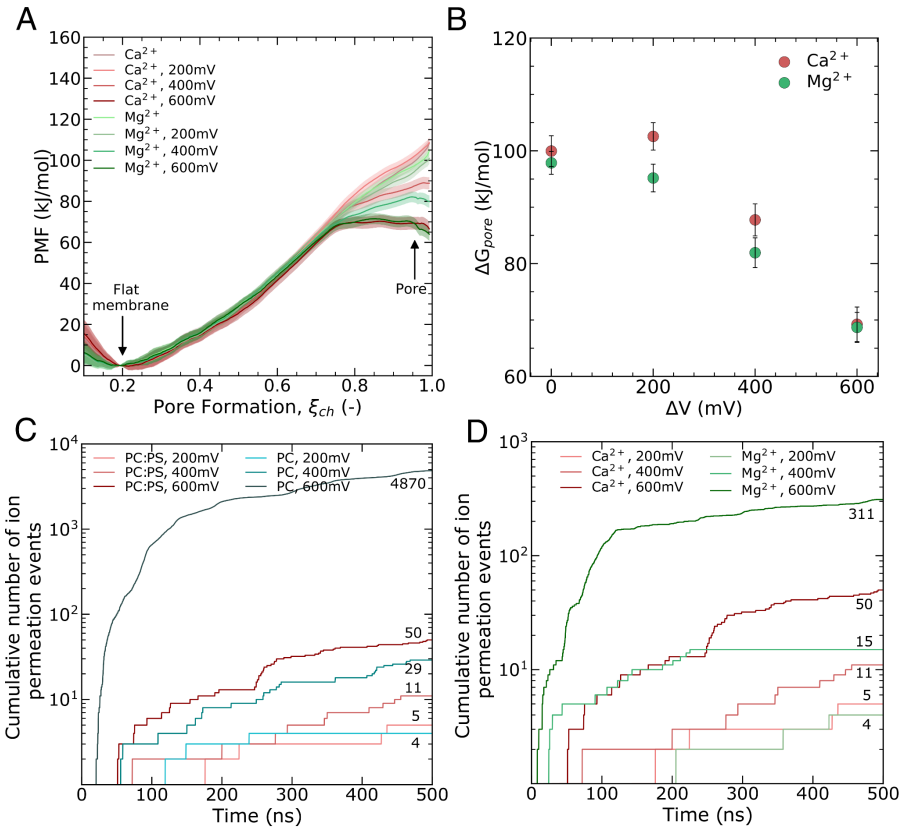

Figure S9: MD simulations of pore formation and ion permeation in presence of Mg^{2+} and Ca^{2+}. Simulations were carried out with Charmm36 lipids with electrostatic continuum correction (Charmm36-ECC). (A) PMFs of pore formation over membranes of POPC:PS 1:1 with increasing membrane potentials between 0 mV and 600 mV, in presence of either Mg^{2+} and Ca^{2+}. (B) Free energy of pore formation taken from PMFs in (A). At given membrane potential, replacing Ca^{2+} with Mg^{2+} leads to a marginal decrease (if any) of the free energies of pore formation ΔG_{pore}. (C) Cumulative number of Ca^{2+} permeation events over membranes of POPC (blue shades) or membranes of POPC:PS 1:1 (red shades) in the presence of restrained open pore. Simulations were carried out with transmembrane potentials of 200, 400, or 600 mV (see legend). The simulations show that (i) Ca^{2+} flux is

reduced in the presence of PS lipids due to stronger binding of Ca^{2+} to the anionic PS headgroups as compared to the zwitterionic PC headgroups, and (ii) the Ca^{2+} flux strongly increases with increasing transmembrane potential. (D) Cumulative number of Mg^{2+} permeation events over a POPC:PS 1:1 membrane with a restrained open pore (green shades). Values for Ca^{2+} permeation events are taken from panel (B) and are shown for reference (red shades).

References

1. Montal, M. & Mueller, P. Formation of Bimolecular Membranes from Lipid Monolayers and a Study of their Electrical Properties. *Proc. Natl. Acad. Sci. U. S. A.* **69**, 3561–3566 (1972).

2. Latorre, R. & Alvarez, O. Voltage-dependent channels in planar lipid bilayer membranes. *Physiol. Rev.* **61**, 77–150 (1981).
3. Weinberger, A. *et al.* Gel-assisted formation of giant unilamellar vesicles. *Biophys. J.* **105**, 154–164 (2013).
4. Macias-Romero, C. *et al.* High throughput second harmonic imaging for label-free biological applications. *Opt. Express* **22**, 31102 (2014).
5. Tarun, O. B., Hannesschläger, C., Pohl, P. & Roke, S. Label-free and charge-sensitive dynamic imaging of lipid membrane hydration on millisecond time scales. *Proc. Natl. Acad. Sci.* **115**, 4081–4086 (2018).
6. Li, L., Li, M., Zhang, Z. & Huang, Z.-L. Assessing low-light cameras with photon transfer curve method. *J. Innov. Opt. Health Sci.* **09**, 1630008 (2016).
7. Tarun, O. B., Okur, H. I., Rangamani, P. & Roke, S. Transient domains of ordered water induced by divalent ions lead to lipid membrane curvature fluctuations. *Commun. Chem.* **3**, 17 (2020).
8. Knight, C. J. & Hub, J. S. MemGen: a general web server for the setup of lipid membrane simulation systems. *Bioinformatics* **31**, 2897–2899 (2015).
9. Jorgensen, W. L., Chandrasekhar, J., Madura, J. D., Impey, R. W. & Klein, M. L. Comparison of simple potential functions for simulating liquid water. *J. Chem. Phys.* **79**, 926–935 (1983).
10. Kohagen, M., Mason, P. E. & Jungwirth, P. Accurate Description of Calcium Solvation in Concentrated Aqueous Solutions. *J. Phys. Chem. B* **118**, 7902–7909 (2014).
11. Mason, P. E., Wernersson, E. & Jungwirth, P. Accurate Description of Aqueous Carbonate Ions: An Effective Polarization Model Verified by Neutron Scattering. *J. Phys.*

Chem. B **116**, 8145–8153 (2012).

12. Duboué-Dijon, E., Mason, P. E., Fischer, H. E. & Jungwirth, P. Hydration and Ion Pairing in Aqueous Mg2+ and Zn2+ Solutions: Force-Field Description Aided by Neutron Scattering Experiments and Ab Initio Molecular Dynamics Simulations. *J. Phys. Chem. B* **122**, 3296–3306 (2018).
13. Kohagen, M., Mason, P. E. & Jungwirth, P. Accounting for Electronic Polarization Effects in Aqueous Sodium Chloride via Molecular Dynamics Aided by Neutron Scattering. *J. Phys. Chem. B* **120**, 1454–1460 (2016).
14. Pastor, R. W. & Mackerell, A. D. J. Development of the CHARMM Force Field for Lipids. *J. Phys. Chem. Lett.* **2**, 1526–1532 (2011).
15. Melcr, J. *et al.* Accurate Binding of Sodium and Calcium to a POPC Bilayer by Effective Inclusion of Electronic Polarization. *J. Phys. Chem. B* **122**, 4546–4557 (2018).
16. Nencini, R. *et al.* Prosecco: polarization reintroduced by optimal scaling of electronic continuum correction origin in MD simulations. Available at: https://gitlab.com/sparkly/prosecco/prosECCo75. Accessed Oct 19, 2022.
17. Essmann, U. *et al.* A smooth particle mesh ewald potential. *J Chem Phys* **103**, 8577–8592 (1995).
18. Bussi, G., Donadio, D. & Parrinello, M. Canonical sampling through velocity rescaling. *J. Chem. Phys.* **126**, 014101 (2007).
19. Parrinello, M. & Rahman, A. Polymorphic transitions in single crystals: A new molecular dynamics method. *J. Appl. Phys.* **52**, 7182–7190 (1981).
20. Miyamoto, S. & Kollman, P. A. SETTLE: An Analytical Version of the SHAKE and RATTLE Algorithms for Rigid Water Models. *J Comp Chem* **13**, 952–962 (1992).
21. Hess, B. P-LINCS: A Parallel Linear Constraint Solver for Molecular Simulation. *J Chem Theory Comput* **4**, 116–122 (2008).
22. Abraham, M. J. *et al.* GROMACS: High performance molecular simulations through multi-level parallelism from laptops to supercomputers. *SoftwareX* **1**, 19–25 (2015).
23. Gumbart, J., Khalili-Araghi, F., Sotomayor, M. & Roux, B. Constant electric field

simulations of the membrane potential illustrated with simple systems. *Biochim. Biophys. Acta BBA - Biomembr.* **1818**, 294–302 (2012).

24. Hub, J. S. & Awasthi, N. Probing a Continuous Polar Defect: A Reaction Coordinate for Pore Formation in Lipid Membranes. *J. Chem. Theory Comput.* **13**, 2352–2366 (2017).

25. Ting, C. L., Awasthi, N., Müller, M. & Hub, J. S. Metastable Prepores in Tension-Free Lipid Bilayers. *Phys. Rev. Lett.* **120**, 128103 (2018).

26. Awasthi, N. & Hub, J. S. Simulations of Pore Formation in Lipid Membranes: Reaction Coordinates, Convergence, Hysteresis, and Finite-Size Effects. *J. Chem. Theory Comput.* **12**, 3261–3269 (2016).

27. Hub, J. S., de Groot, B. L. & van der Spoel, D. g_wham—A Free Weighted Histogram Analysis Implementation Including Robust Error and Autocorrelation Estimates. *J. Chem. Theory Comput.* **6**, 3713–3720 (2010).

28. Kumar, S., Rosenberg, J. M., Bouzida, D., Swendsen, R. H. & Kollman, P. A. THE weighted histogram analysis method for free-energy calculations on biomolecules. I. The method. *J. Comput. Chem.* **13**, 1011–1021 (1992).

29. Paula, S., Volkov, A. G., Van Hoek, A. N., Haines, T. H. & Deamer, D. W. Permeation of protons, potassium ions, and small polar molecules through phospholipid bilayers as a function of membrane thickness. *Biophys. J.* **70**, 339–348 (1996).

30. Leontiadou, H., Mark, A. E. & Marrink, S.-J. Ion Transport across Transmembrane Pores. *Biophys. J.* **92**, 4209–4215 (2007).

31. Kleinzeller, A. Chapter 1 Charles Ernest Overton's Concept of a Cell Membrane. in *Membrane Permeability: 100 Years Since Ernest Overton* (eds. Deamer, D. W., Kleinzeller, A. & Fambrough, D. M.) vol. 48 1–22 (Academic Press, 1999).

32. Eisenberg, D. & Crothers, D. *Physical Chemistry: with Applications to the Life Sciences*. (1979).

33. Kamp, F. & Hamilton, J. A. pH gradients across phospholipid membranes caused by fast flip-flop of un-ionized fatty acids. *Proc. Natl. Acad. Sci.* **89**, 11367–11370 (1992).

34. Vorobyov, I. *et al.* Ion-Induced Defect Permeation of Lipid Membranes. *Biophys. J.*

106, 586–597 (2014).

35. Tepper, H. L. & Voth, G. A. Mechanisms of Passive Ion Permeation through Lipid Bilayers: Insights from Simulations. *J. Phys. Chem. B* **110**, 21327–21337 (2006).

36. Fathizadeh, A. & Elber, R. Ion Permeation through a Phospholipid Membrane: Transition State, Path Splitting, and Calculation of Permeability. *J. Chem. Theory Comput.* **15**, 720–730 (2019).

37. Mansy, S. S. Membrane Transport in Primitive Cells. *Cold Spring Harb. Perspect. Biol.* **2**, a002188–a002188 (2010).

38. Kamiya, K., Kawano, R., Osaki, T., Akiyoshi, K. & Takeuchi, S. Cell-sized asymmetric lipid vesicles facilitate the investigation of asymmetric membranes. *Nat. Chem.* **8**, 881–889 (2016).

39. LeBarron, J. & London, E. Effect of lipid composition and amino acid sequence upon transmembrane peptide-accelerated lipid transleaflet diffusion (flip-flop). *Biochim. Biophys. Acta BBA - Biomembr.* **1858**, 1812–1820 (2016).

40. Marcus, Y. Thermodynamics of solvation of ions. Part 5.—Gibbs free energy of hydration at 298.15 K. *J Chem Soc Faraday Trans* **87**, 2995–2999 (1991).

41. Khavrutskii, I. V., Gorfe, A. A., Lu, B. & McCammon, J. A. Free Energy for the Permeation of Na+ and Cl− Ions and Their Ion-Pair through a Zwitterionic Dimyristoyl Phosphatidylcholine Lipid Bilayer by Umbrella Integration with Harmonic Fourier Beads. *J. Am. Chem. Soc.* **131**, 1706–1716 (2009).

42. Neale, C., Madill, C., Rauscher, S. & Pomès, R. Accelerating Convergence in Molecular Dynamics Simulations of Solutes in Lipid Membranes by Conducting a Random Walk along the Bilayer Normal. *J. Chem. Theory Comput.* **9**, 3686–3703 (2013).

43. Verbeek, S. F. *et al.* How arginine derivatives alter the stability of lipid membranes: dissecting the roles of side chains, backbone and termini. *Eur. Biophys. J.* **50**, 127–142 (2021).

44. Awasthi, N. *et al.* Molecular Mechanism of Polycation-Induced Pore Formation in Biomembranes. *ACS Biomater. Sci. Eng.* **5**, 780–794 (2019).

45. Boyd, R. W. *Nonlinear Optics*. (Academic Press, 2008).